Trans. Phenom. Nano Micro Scales, 6(2): 133-151, Summer and Autumn 2018
DOI: 10.22111/tpnms.2018.16509.1100

ORIGINAL RESEARCH PAPER

Three dimensional numerical study on a trapezoidal microchannel heat sink with different inlet/outlet arrangements utilizing variable properties nanofluid

Hossein Khorasanizadeh*, Mojtaba Sepehrnia

Faculty of Mechanical Engineering and the Energy Research Institute, University of Kashan, Kashan, Iran

Received 23 September 2016; revised 11 November 2017; accepted 7 January 2018; available online 3 july 2018

ABSTRACT: Nowadays, microchannels as closed circuits channels for fluid flow and heat removal are an integral part of the silicon-based electronic microsystems. Most of previous numerical studies on microchannel heat sinks (MCHS) have been performed for a two-dimensional domain using constant properties of the working fluid. In this study, laminar fluid flow and heat transfer of variable properties Al_2O_3-water nanofluid in a trapezoidal MCHS, consisted of five trapezoidal microchannels have been studied. The three dimensional solution domains include the whole flow field and the complete MCHS solid parts. Four inlet/outlet arrangements, three pressure drops of 5, 10 and 15 kPa and nanoparticles volume fractions between 0 and 4% are assumed and the effects of these arrangements, properties variations and the Brownian motion on the heat sink performance quantified. The results indicate that the A-type heat sink, for which the inlet and outlet are placed horizontally at the center of the north and the south walls, has a better heat transfer performance, smaller thermal resistance and provides more uniform substrate temperature distribution. Temperature-dependent properties increases the heat transfer between 2.7% and 3.39%, decreases the thermal resistance between 3.49% and 6.29 % and decreases the ratio of difference between the maximum and minimum substrate temperatures to the heat flux between 3.3% and 7.19%. Presence of the Brownian motion showed a similar trend but with a slighter importance.

KEYWORDS: *Inlet/outlet arrangements; KKL Brownian motion model; Trapezoidal microchannel; Trapezoidal heat sink; Variable properties nanofluid*

INTRODUCTION

Generation of high heat fluxes in very large scale integrated (VLSI) circuits necessitates a proper thermal management strategy. Otherwise, the increased substrate temperature may lead to collapse of any electronic device. The concept of microchannel heat sink (MCHS) was firstly proposed by Tuckerman and Pease (1) in 1981. They investigated a microchannel heat sink utilizing water as the coolant. Nowadays, microchannels, as closed circuits channels for fluid flow and heat removal are an integral part of the silicon-based electronic microsystems. Microchannels, with variety of cross sections and hydraulic diameters, provide many benefits such as higher heat transfer area per unit volume, high heat transfer coefficients and lower coolant requirement (1), when compared with the conventional and millimeter sized channels. Wu and Cheng (2) measured the laminar flow friction factor of deionized water in smooth silicon trapezoidal cross-section microchannels with hydraulic diameters in the range of 25.9–291 μm, experimentally. They showed that the friction constant (f×Re) of these microchannels is greatly influenced by the cross sectional aspect ratio. Chein and Huang (3) analyzed performance of a silicon based microchannel heat sink using constant properties nanofluids as coolant. They showed that the presence of nanoparticles, with small particle size and low volume fract-ion, enhanced heat transfer but did not produce extra pressure drop.

Abbassi (4) studied entropy generation in a rectangular microchannel heat sink, analytically. He used water, ethylene glycol, fluorocarbon and ethanol as working fluids. In order to investigate the local entropy generation characteristics in MCHS and to find out under what conditions entropy generation can be minimized, he utilized the porous medium approach. He found that entropy generation rate in MCHS is a strong function of microchannel aspect ratio, thermal conductivity ratio and porosity and is a weak function of Peclet number. Also, he showed that the best thermal performance occurs when the channel aspect ratio was the maximum.

Niazmand et al. (5) investigated slip-flow and heat transfer in trapezoidal microchannels. They showed that in the fully developed region, the friction coefficient (f) decreases strongly with increasing both of Knudsen number and aspect ratio, but it has a weaker dependence on the side angle.

Shams et al. (6) simulated the slip flow through rhombus microchannels numerically. Their results showed that aspect ratio and Knudsen number have important impact on Poiseuille and Nusselt numbers in such microchannels. Although variation of viscosity of liquids with temperature is more than that for gases, still viscosity variation of gases must be considered. However, in their two dimensional study this was not considered.

*Corresponding Author Email: *khorasan@kashanu.ac.ir*
Tel.: +98 3155912449; Note. This manuscript was submitted on September 23, 2016; approved on November 11, 2017; published online july 3, 2018.

Nomenclature

A	Area (m^2)	ρ	Density (kg m^3)
c_p	Specific heat (J $kg^{-1}K^{-1}$)	μ	Viscosity (kg m^{-1} s^{-1})
D_h	Hydraulic diameter (m)	κ_b	Boltzman constant (J K^{-1})
D	Diameter (m)	θ	The maximum temperature difference on substrate surface per unit heat applied (K m^2 W^{-1})
k	Thermal conductivity (W $m^{-1}K^{-1}$)		
L	Length (m)		**Subscripts**
$\dot{m}$	Mass flow rate (kg s^{-1})	avg	average
$\overline{Nu}$	Average Nusselt number	b	base plate
P	Pressure (kPa)	ch	channel
P	Wet perimeter (m)	eff	effective
Q_{flow}	Heat absorbed by fluid (W)	f	base fluid
Q	Heat flux (W/m^2)	fin	fin
		hs	heat sink
	Greek Symbols	in	inlet
Φ	Volume fraction of nanoparticles	max	maximum

Chein and Chen (7) used water as the working fluid and studied inlet/outlet arrangement effects on a rectangular microchannel heat sink performance, numerically. They used 6 different arrangements named I-, N-, D-, S-, U- and V-types. In the I-, N-, D- and S-types, fluid flow was supplied and collected horizontally, while in the U- and V-type the flow was supplied and collected vertically. They showed for the heat sinks with horizontally fluid supply and collection, the velocity misdistribution through different microchannels was more serious than those of vertically flow supply and collection. They studied the thermal resistance, overall heat transfer coefficient and pressure drop coefficient to quantify the heat sink performance and found that the heat sink with vertically fluid supply and collection perform better.

Hung and Yan (8) studied the effect of tapered-channel design on thermal performance of microchannel heat sink, numerically.

They found that the relationship between the thermal resistance and the width-tapered ratio is not monotonic at the fixed pumping power, since the thermal resistance first decreased and then increased. A similar behavior was also exhibited by the height-tapered ratio. It was also found that the width-tapered channel design has a lower and a relatively uniform temperature distribution along channel centerline compared to those of parallel or height-tapered channel designs.

Izadi et al. (9) numerically studied laminar forced convection of a Al_2O_3–water nanofluid flowing in a micro heat sink. They showed that Nusselt number increases with volume fraction enhancement. Also they found that solid material has no effect on pressure drop increment.

Mashaei et al. (10) investigated the effect of nanoparticles on laminar forced convection in a serpentine microchannel, numerically. They found that when the applied heat flux increases, the heat transfer rate increases and the pressure drop decreases. Also they showed that the best thermal-hydraulic performance occurs at the lowest Reynolds number and medium nanoparticle volume fraction.

Ting et al. (11) employed the stream wise conduction term in the energy equation and analytically studied the entropy generation of Al_2O_3–water nanofluid flow in microchannels. They showed that the stream wise conduction prominently affects the thermal characteristics of the nanofluid and consequently the entropy generation and its heat transfer irreversibility component, which is intimately associated with the streamwise conduction. Ignoring variable properties and the Brownian motion are two deficiencies of this study.

Leela Vinodhan and Rajan (12) numerically studied new microchannel heat sink designs. They utilized water as the working fluid and divided the heat sink into four quadrants, each with a separate inlet and outlet. After some minor modification with respect to the microchannel length, they used the I-type heat sink of Chein and Chen (7) as the conventional heat sink. They showed that, because of more uniform distribution of coolant, the bottom plate temperature gradients in the new microchannel heat sink designs are lower than that in conventional heat sink.

Also they found thermal resistances of the new microchannel heat sink designs are lower than the thermal resistance in conventional heat sink. Utilization of independent properties is the deficiency of this study.

Fani et al. (13) studied the effect of the Brownian motion and the viscous dissipation on the laminar forced convection of copper-oxide nanofluid in a trapezoidal MCHS using the Eulerian–Eulerian two-phase approach. They observed that the Brownian motion depends on nanofluid inlet temperature, nanoparticles diameter and volume fraction of nanoparticles.

Duryodhan et al. (14) studied convective heat transfer in diverging and converging three-dimensional microchannels experimentally; also they performed three dimensional numerical simulations. Their numerical results showed that the conjugate effect causes different nature of heat flux

distribution in diverging versus converging microchannels. This led to a nearly constant heat flux condition and 35% higher heat transfer in converging microchannel compared with that of diverging one. Their results showed that diverging and converging microchannels exhibit better thermo-hydraulic performance over uniform cross-section microchannels. Hence, these types of microchannels can be useful in the design of micro-devices employed in chemical, biological and electronics cooling applications, which involve single phase liquid heating.

Dehghan et al. (15) studied heat transfer enhancement in converging flow passage rectangular MCHS utilizing water. Their results showed that the Poiseuille number increased with increased tapering, while the required pumping power decreased. Also, with tapering the Nusselt number as well as the convection heat transfer coefficient increased.

Yue et al. (16) numerically studied Al_2O_3–water nanofluid flow in a rectangular manifold MCHS. They noted that with increasing volume fraction of Al_2O_3–water nanofluid and depending on the condition, the performance index either increases or decreases. Also they found for reducing the total entropy generation and to improve the performance index, nanoparticles with small diameter should be utilized.

Based on the findings of the previous studies, heat transfer from the solid to fluid in a microchannel heat sink increases by: increasing heat transfer surface using fins (17), using porous media (18), enhancing thermal conductivity of the coolant (19), optimizing the design of the microchannel heat sink (20-22), optimizing the cross-section of microchannel (23) and using proper flow inlet/outlet arrangements (7). Heat transfer has been a great challenge for industrial applications as well as for engineering research in order to achieve better efficiency. Nanofluids have demonstrated better thermal characteristics; thus are suitable for high heat flux systems such as electronic cooling systems, liquid heat exchangers, solar systems and nuclear reactors. Several cases related to the application of nanofluids in microchannels for cooling the electronic devices have been presented in (24-27). Kazemi-Beydokhti and Heris (28) utilized nanofluids in a CHP system and showed utilization of nanofluids increases the CHP performance. Ali et al. (29) investigated convective heat transfer performance of ZnO-water nanofluid in the car radiator, experimentally. They used different volumetric concentrations to find the optimum volume fraction for thermal enhancement. They observed heat transfer enhancement up to 46% by utilizing ZnO-water nanofluid with nanoparticles volume fraction of 0.2% compared to that of the base fluid. Some more advantages of utilizing nanofluids for solar energy storage purposes have been displayed in (30-33).

In most of the previous studies on MCHS, the computational domain consisted only of a single channel and a corresponding slice of a fin, for which symmetrical boundary condition was used. Also previous studies on the effects of different inlet/outlet arrangements on performance of microchannel heat sinks are limited to rectangular microchannel heat sinks and water as the coolant. A MCHS with trapezoidal geometry may be used for cooling electronic chips which are sited in an unwanted trapezoidal space. So, in the present study, for a trapezoidal MCHS consisting of five trapezoidal microchannels, the three dimensional computational domain includes the geometric configuration and location of the inlet and outlet and the complete flow passage through microchannels (inlet, inlet plenum, five microchannels, outlet plenum and outlet) and the solid parts of the heat sink (base plate, side walls and fins). The effects of different inlet/outlet arrangements on the MCHS performance, which has rarely been considered, are investigated. For this purpose Al_2O_3–water nanofluid is employed, its properties variation with temperature and the Brownian motion are considered and their effects are quantified.

GEOMETRIC CONFIGURATIONS

The geometric configuration and general dimensions of the A-type trapezoidal microchannel heat sink and the microchannels, for which the horizontal inlet and outlet are situated at the center of the north and the south walls, respectively, are shown in Figure 1.

As indicated in Figure 2, the heat sink consists of 5 isosceles trapezoidal microchannels numbered from the left to the right. According to channel classification scheme, channels having diameter greater than 10 micrometer and less than 200 micrometer are referred to as microchannels (34).

In the present work, the trapezoidal microchannels have a hydraulic diameter of 198 μm. In practice, the electronic chip, which generates heat, is directly attached to the base plate (substrate) of the heat sink. All solid parts of the heat sink are made of silicon and the working fluid is considered to be Al_2O_3–water nanofluid.

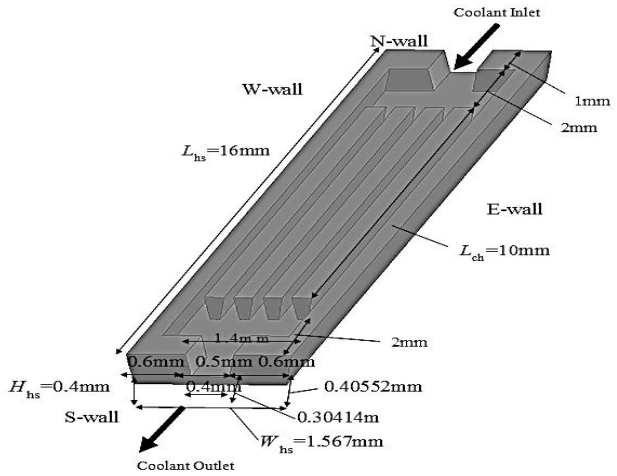


Fig. 1. Geometric configuration of the A-type microchannel heat sink

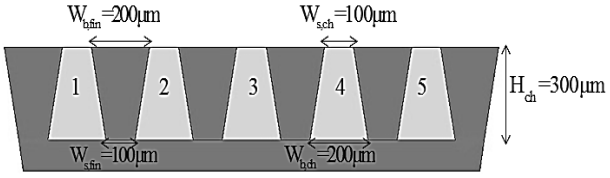


Fig. 2. Fin and microchannel dimensions

To investigate the effects of inlet/outlet arrangement on heat transfer and fluid flow, in addition to the previously specified arrangement, three other arrangements have been considered.

As shown in Figure 3, these arrangements are called the B-, C- and D-type, respectively. Other than change of inlet/outlet locations, all of the geometric dimensions of these types are the same as those shown in Figure 1 for the A-type configuration.

In the B-type heat sink, the inlet and outlet have been moved from the centers of the north and south walls to the right edge of the inlet plenum and the left edge of the outlet plenum, respectively.

In the C-type heat sink, the inlet and outlet are located on the west wall at the center of the inlet and outlet plenums. In the D-type heat sink, the inlet is on the east wall at the center of the inlet plenum, but the outlet is on the west wall at the center of the outlet plenum.

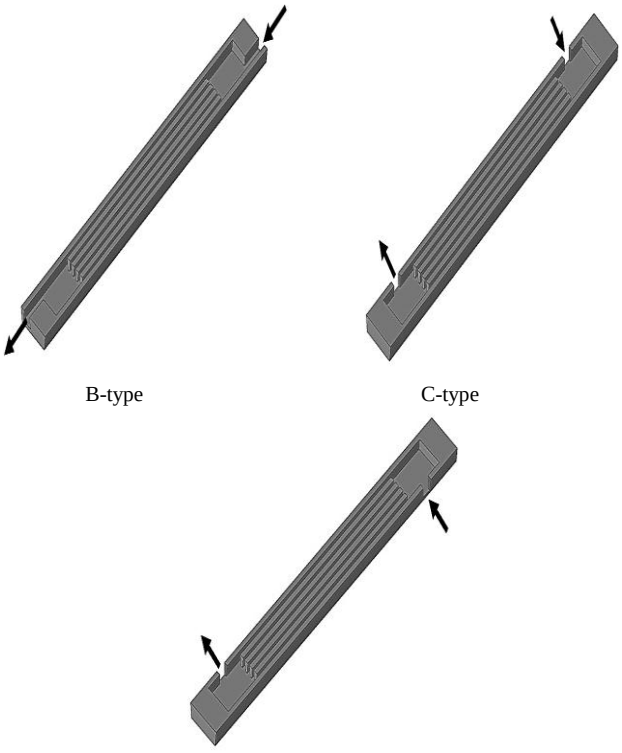


Fig. 3. The geometry showing the B-, C- and D-type inlet/outlet arrangements

THE GOVERNING EQUATIONS AND BOUNDARY CONDITIONS

To drive the governing equations for the fluid flow and heat transfer, the following assumptions have been taken into account:

1. Fluid flow and heat transfer are steady and three dimensional.
2. The nanofluid is assumed a single phase, incompressible and the flow is laminar.
3. The properties of the nanofluid and the heat sink solid parts are temperature dependent.
4. The exposed surfaces of heat sink to the surroundings including the side walls and the top wall which creates the flow passage in every microchannel are insulated.

According to the above assumptions, the governing equations are:

Continuity:

$$\frac{\partial}{\partial x}\left(\rho_{nf}u\right)+\frac{\partial}{\partial y}\left(\rho_{nf}v\right)+\frac{\partial}{\partial z}\left(\rho_{nf}w\right)=0 \tag{1}$$

Momentum:

$$\frac{\partial}{\partial x}\left(\rho_{nf}uu\right)+\frac{\partial}{\partial y}\left(\rho_{nf}vu\right)+\frac{\partial}{\partial z}\left(\rho_{nf}wu\right)= -\frac{\partial p}{\partial x}+\frac{\partial}{\partial x}\left(\mu_{nf}\frac{\partial u}{\partial x}\right)+\frac{\partial}{\partial y}\left(\mu_{nf}\frac{\partial u}{\partial y}\right)+\frac{\partial}{\partial z}\left(\mu_{nf}\frac{\partial u}{\partial z}\right) \tag{2}$$

$$\frac{\partial}{\partial x}\left(\rho_{nf}uv\right)+\frac{\partial}{\partial y}\left(\rho_{nf}vv\right)+\frac{\partial}{\partial z}\left(\rho_{nf}wv\right)= -\frac{\partial p}{\partial y}+\frac{\partial}{\partial x}\left(\mu_{nf}\frac{\partial v}{\partial x}\right)+\frac{\partial}{\partial y}\left(\mu_{nf}\frac{\partial v}{\partial y}\right)+\frac{\partial}{\partial z}\left(\mu_{nf}\frac{\partial v}{\partial z}\right) \tag{3}$$

$$\frac{\partial}{\partial x}\left(\rho_{nf}uw\right)+\frac{\partial}{\partial y}\left(\rho_{nf}vw\right)+\frac{\partial}{\partial z}\left(\rho_{nf}ww\right)= -\frac{\partial p}{\partial z}+\frac{\partial}{\partial x}\left(\mu_{nf}\frac{\partial w}{\partial x}\right)+\frac{\partial}{\partial y}\left(\mu_{nf}\frac{\partial w}{\partial y}\right)+\frac{\partial}{\partial z}\left(\mu_{nf}\frac{\partial w}{\partial z}\right) \tag{4}$$

Energy in the fluid part:

$$\frac{\partial}{\partial x}\left(\rho_{nf}uT\right)+\frac{\partial}{\partial y}\left(\rho_{nf}vT\right)+\frac{\partial}{\partial z}\left(\rho_{nf}wT\right)= \frac{\partial}{\partial x}\left(\frac{k_{nf}}{c_{p_{nf}}}\frac{\partial T}{\partial x}\right)+\frac{\partial}{\partial y}\left(\frac{k_{nf}}{c_{p_{nf}}}\frac{\partial T}{\partial y}\right)+\frac{\partial}{\partial z}\left(\frac{k_{nf}}{c_{p_{nf}}}\frac{\partial T}{\partial z}\right) \tag{5}$$

Energy in the solid parts:

$$\frac{\partial}{\partial x}\left(k_s\frac{\partial T}{\partial x}\right)+\frac{\partial}{\partial y}\left(k_s\frac{\partial T}{\partial y}\right)+\frac{\partial}{\partial z}\left(k_s\frac{\partial T}{\partial z}\right)=0 \tag{6}$$

The boundary conditions are related to the heat sink operational conditions.

In practical applications, to receive heat and dissipate it by the fluid flow, heat sink is attached to a heat generation source such as an electronic chip.

The fluid at a given temperature and mass flow rate is provided by an external pump.

Since pressure drop is related to flow rate, either flow rate or pressure drop can be taken as a constants for the simulation. In this study, similar to the study of Li et al. (35), the pressure drop is adopted a constant.

According to operating conditions explained above, the boundary conditions for the governing equations are:
Inlet:

$$p = p_{\text{in}}, \qquad T = T_{\text{in}} \tag{7}$$

Outlet:

$$\frac{\partial T}{\partial n} = 0, \quad p = p_{\text{out}}, \tag{8}$$

Fluid-solid interfaces:

$$\vec{V} = 0, \quad T_{\text{f}} = T_{\text{s}}, \quad -k_{\text{s}} \frac{\partial T_{\text{s}}}{\partial n} = -k_{\text{f}} \frac{\partial T_{\text{f}}}{\partial n} \tag{9}$$

At the base plate:

$$q_{\text{w}} = -k_{\text{s}} \frac{\partial T_{\text{s}}}{\partial n} \tag{10}$$

p_{in} and T_{in} are the fluid inlet pressure and temperature, respectively. p_{out} is the outlet pressure, n is the direction normal to the specified wall or the outlet plane. The base plate of heat sink is subjected to a heat flux of q_{w}=200 kW/m^2.

This value has been picked because of admissible temperature range of the nanofluid property relations utilized. The pressure drop across the heat sink is defined as $\Delta p = p_{\text{in}} - p_{\text{out}}$.

As seen from Equation 9, the non-slip condition has been assumed for every solid-liquid interface.

Thermophysical properties of the nanofluid

The density of the nanofluid based on volume fraction of nanoparticles is determined by (36):

$$\rho_{nf} = (1-\varphi)\rho_{\text{f}} + \varphi\rho_{\text{p}} \tag{11}$$

The subscripts p and f refer to nanoparticle and the base fluid, respectively. The base fluid is pure water, and φ is the volume fraction of Al_2O_3 nanoparticles, $\varphi = V_{\text{p}}/(V_{\text{p}}+V_{\text{f}})$. By considering thermal equilibrium between the base fluid and the nanoparticles, the heat capacity of nanofluid is (37):

$$\left(\rho c_{\text{p}}\right)_{nf} = (1-\varphi)\left(\rho c_{\text{p}}\right)_{\text{f}} + \varphi\left(\rho c_{\text{p}}\right)_{\text{p}} \tag{12}$$

The effective thermal conductivity of nanofluid, achieved based on the Brownian motion effect, is:

$$k_{nf} = k_{\text{static}} + k_{\text{Brownian}} \tag{13}$$

This description has been found to agree very well with the experimental data (38,39) and takes into consideration the nanoparticles size, volume fraction, types of the nanoparticles and the base fluid. The static part is that of Hamilton-Crosser model (40) and dynamic part is that of Koo-Kleinstreuer-Li (KKL) model (41), which is based on kinetic theory.

$$k_{\text{static}} = k_{\text{f}}\left[\frac{\left(k_{\text{p}} + 2k_{\text{f}}\right) - 2\varphi\left(k_{\text{f}} - k_{\text{p}}\right)}{\left(k_{\text{p}} + 2k_{\text{f}}\right) + \varphi\left(k_{\text{f}} - k_{\text{p}}\right)}\right] \tag{14}$$

Where k_{f} and k_{p} are the thermal conductivity of the base fluid and the nanoparticles, respectively.

The dynamic part is:

$$k_{\text{brownian}} = 5\times10^4 \varphi\rho_{\text{f}} c_{\text{p,f}} \sqrt{\frac{\kappa_{\text{b}} T}{d_{\text{p}}\rho_{\text{p}}}}\, g\left(T, \varphi, d_{\text{np}}\right) \tag{15}$$

Where ρ_{f} and $c_{\text{p,f}}$ are the density and the heat capacity of the base fluid, respectively. Also ρ_{p} and φ are the density and volume fraction of nanoparticles, respectively and κ_B is the Boltzman constant equal to 1.3807×10^{-23} J/K.

The function g for Al_2O_3-water nanofluid is (41):

$$g\left(T, \varphi, d_{\text{np}}\right) = \begin{pmatrix} a + b\ln\left(d_{\text{np}}\right) + \\ c\ln(\varphi) + \\ d\ln(\varphi)\ln\left(d_{\text{np}}\right) + \\ e\ln\left(d_{\text{np}}\right)^2 \end{pmatrix} \ln(T) + \begin{pmatrix} m + h\ln\left(d_{\text{np}}\right) + i\ln(\varphi) + \\ j\ln(\varphi)\ln\left(d_{\text{np}}\right) + k\ln\left(d_{\text{np}}\right)^2 \end{pmatrix} \tag{16}$$

The magnitudes of different coefficients in Equation16 are given in Table 1. The Equation16 for Al_2O_3–water nanofluid has a correlation coefficient of 96% (41).

The importance of the interfacial resistance (Kapitza resistance) (42,43), which has an evident effect on weakening the effective thermal conductivity between the adjacent layers of two different materials, should be taken into consideration. The relation between the effective nanoparticle thermal conductivity and the nanoparticle thermal conductivity in static part is:

$$R_b + \frac{d_p}{k_p} = \frac{d_p}{k_{p,eff}} \tag{17}$$

Where d_p is nanoparticle diameter and R_b=4×10^{-8}Km^2/W (44).

The effective viscosity of nanofluids is expressed as (29):

$$\mu_{eff} = \mu_{static} + \mu_{Brownian} \tag{18}$$

Table 1
The magnitude of coefficients in Equation16 for Al_2O_3–water (41).

Coefficient	magnitude	coefficient	magnitude
a	52.813488759	*m*	-298.19819084
b	6.115637295	*h*	-34.532716906
c	0.695574508	*i*	-3.9225289283
d	4.1745555278e-2	*j*	-0.2354329626
e	0.176919300241	*k*	-0.999063481

The static and dynamic parts of Equation18 are evaluated as (45):

$$\mu_{static} = \frac{\mu_f}{(1-\varphi)^{2.5}} \tag{19}$$

$$\mu_{Brownian} = 5\times10^4 \varphi\rho_f \sqrt{\frac{\kappa_b T}{d_p\rho_p}}\, g(T,\varphi,d_{np}) \tag{20}$$

The thermo-physical properties of pure water taken from (46) , within the temperature range of 300 to 325 K, have been curve fitted by MATLAB using the exponential method with a correlation coefficient of 95%.

Also the temperature dependent thermal conductivity of silicon has been taken from (47).

The results are:

$$k_f = 0.3424\exp(0.00195T) - 0.00163 \tag{21}$$

$$\mu_f = 57.83\exp(-0.04053T) + 0.01473\exp(-0.01095T) \tag{22}$$

$$\rho_f = 1130\exp(-0.0004173T) \tag{23}$$

$$c_{p,f} = 6.747\times10^8 \exp(-0.05862T) + 3989\exp(0.0001428T) \tag{24}$$

$$k_{silicon} = 290 - 0.4T \tag{25}$$

The thermo-physical properties of the base fluid and Al_2O_3 nanoparticles at 300 K are presented in Table 2 (48).

PERFORMANCE EVALUATION INDEXES

To evaluate the overall performance of the heat sink several indexes are utilized normally.
These indexes are explained in the following sub sections.

Average Nusselt number

According to Newton's law of cooling, the total heat transfer in a heat sink is:

$$q_w = \bar{h}(T_{hs,avg} - T_{avg}) \tag{26}$$

Where $T_{hs,avg}$ and T_{avg} are the overall average temperatures of heat sink and coolant, respectively.

The average Nusselt number, as a thermal performance index, is defined as:

$$\overline{Nu} = \frac{\bar{h} D_h}{k_f} \tag{27}$$

Where $\bar{h}$ is the heat transfer coefficient, which is calculated via Equation 26, and D_h is the hydraulic diameter of every channel evaluated as:

$$D_h = \frac{4A}{p} \tag{28}$$

Total thermal resistance

The total thermal resistance of microchannel heat sink is

Table 2
Thermo-physical properties of the base fluid and the nanoparticles at 300 K (48).

	$k(wm^{-1}K^{-1})$	$c_p(J\,kg^{-1}K^{-1})$	$\rho(kg\,m^{-3})$
Water	0.613	4179	997
Al_2O_3 nanoparticles	40	765	3970

consisted of conductive and convective resistances (49). The conductive resistance is independent of pressure drop, while the convective resistance decreases with increasing pressure drop (49). The total thermal resistance of the heat sink is:

$$R_{th} = \frac{T_{w,max} - T_{in}}{q_w W_{hs} L_{hs}} \quad (29)$$

Where $T_{w,max}$ is the heat sink base plate maximum temperature.

Non-uniformity of base plate temperature

Decreasing the temperature of the base plate is an important objective of designing new configurations for microchannel heat sinks.

Difference between the maximum and the minimum base plate temperatures is smaller when the cooling is more uniform. Theta is the ratio of difference between the maximum and minimum base plate temperatures to the heat flux, defined as:

$$\theta = \frac{T_{b,max} - T_{b,min}}{q_w} \quad (30)$$

θ is regarded as the measure of non-uniformity of the base plate temperature.

NUMERICAL PROCEDURE

The three-dimensional governing equations with the associated boundary conditions for the fluid flow and heat transfer have been solved using the finite volume method and SIMPLE algorithm. In the following two sections the results of validation and mesh refinement studies are presented.

VALIDATION

In order to make sure about the validity of the computational method and the numerical results, solutions were obtained for the three dimensional MCHS used in the numerical study of Chein and Chen (7) also in the experimental study of Phillips (50).

A three dimensional heat sink geometry completely similar to that of studies of Chein and Chen (7) and Phillips (50) was considered and water was utilized as the working fluid.

As shown in Figure 4, the MCHS utilized for the validation study consists of 11 rectangular microchannels. For the validation study three pressures drops of 25, 35 and 50 kPa and the heat flux of 1000 kW/m^2 were assumed and a grid system with 891372 elements utilized. The average Nusselt number values obtained in this study have been compared with those of Chein and Chen in Figure 5a.

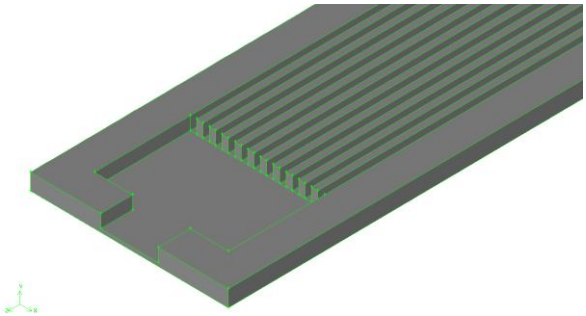
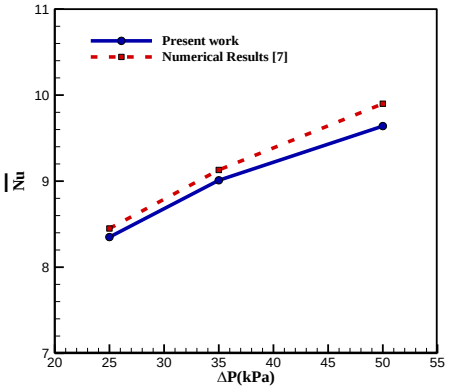
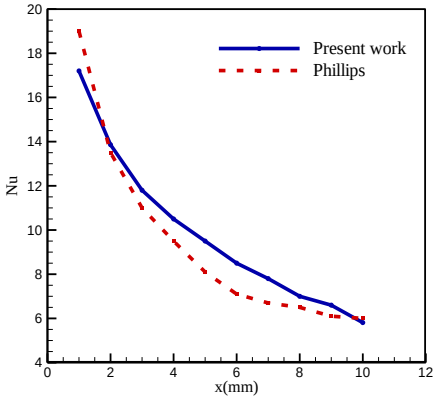


Fig. 4. The geometry of Chein and Chen (7) and Philips (50); utilized here for the validation study

Also in Figure 5b the local Nusselt number values along the microchannel #5 have been compared with those of Philips (50) for the pressure drop of 50 kPa. The trend of local Nusselt number change along microchannel #5 is the same as that of Philips. Also the maximum relative difference between the average Nusslet number obtained in this study and that of Chein and Chen is less 3%, which is for pressure drop of 50 kPa. Thus the validity of the computational method and the numerical results of this study are stated.



(a)



(b)

Fig. 5. Comparison between the results of present work and numerical results of Chein and Chen (7) & experimental results of Philips (50): a) average Nusselt number for three pressure drops b) local Nusselt number along microchannel #5, ΔP=50 kPa

Grid independency test

To check the mesh independency of the results, solutions have been obtained by utilizing three different grid systems, presented in Table 3 for the A-type heat sink, ΔP=15 kPa, q_w=200 kW/m^2 and the working fluid has been assumed to be water. Cubical meshes have been used, subject to the angle of trapezoid sides.

As reported in Table 3, the average Nusselt number for very fine grid is only 0.34% higher than that of fine grid; therefore the grid system with 673920 elements seems to be fine enough.

In order to ensure the independence of the results from the selected grid, temperature along bottom center of microchannel #3(fluid-solid interface) in A-type MCHS, obtained using the same grid systems, have been shown in Figure 6.

The results state that for the A-type MCHS the fine grid system is appropriate.

Table 3
The average Nusselt number for water and A-type heat sink utilizing different numbers of grids; ΔP=15 kPa and q_w=200 kW/m^2.

	Total number of grids	Grids in different directions	Average Nusselt number	Relative difference%
Coarse	391680	192×40×72	14.299	-
Fine	673920	240×48×72	14.846	3.82
Very fine	1365840	288×56×104	14.897	0.34

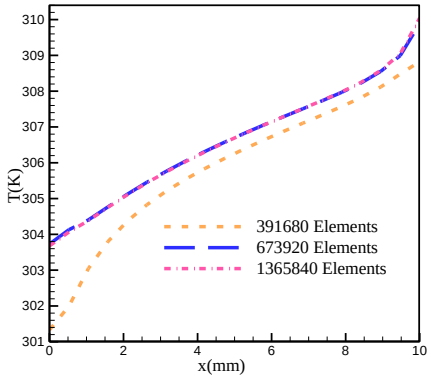


Fig. 6. Temperature along bottom center of microchannel #3 in A-type MCHS using three different grids; ΔP=15 kPa and q_w=150 kW/m^2

It should be noted that from the sum of 673920 elements, 406080 elements are in the solid part and 267840elements are in the fluid part. The same grid density was therefore adopted and used for all further simulations.

As assumed by Chein and Chuang (51), if heat loss to the environment is neglected, the energy absorbed by the working fluid is:

$$Q_{\text{flow}} = \dot{m} c_p \left(T_{\text{out}} - T_{\text{in}}\right) \quad (31)$$

Where $\dot{m}$ is the mass flow rate and T_{in} and T_{out} are the nanofluid inlet and outlet temperatures, respectively. In theory, at steady state conditions the absorbed heat rate by the working fluid across the heat sink must be equal to the applied heat rate. However, the numerical solutions commonly show a small difference, which can be attributed to the utilized grid system. For instance, the maximum relative difference between the absorbed and applied heat rates in the study of Chein and Chen (7) for straight inlet/outlet arrangement was 5.4%. To find which heat sink geometry, in terms of inlet/outlet arrangement, is more critical based on the difference between the applied and removed heat rates, solutions were obtained for all of the heat sink types. For this purpose water was used as the working fluid under ΔP=15 kPa and q_w=200 kW/m^2 and almost the same number of grids were utilized for all of the nominated types. In Table 4, the percentage of relative difference between the applied heat rate to the heat sink and the heat absorbed have been presented for four types of heat sinks employed. It should be noted that the difference between the maximum and the minimum mesh numbers is only 44280, which is acceptable according to the range of the utilized number of meshes. The maximum relative difference between the absorbed and applied heat rates is 5.42%, which is for the A-type heat sink, indicating that the most crucial type is the A-type heat sink. This restates that the grid system having around 673920 elements, utilized for the A-type heat sink, is suitable for the other types; , hence has been used for all of further simulations.

RESULTS AND DISCUSSION

The simulations have been performed for Al_2O_3–water nanofluid with nanoparticles diameter of 25 nm, volume fraction of 0, 2 and 4%, pressure drops of 5, 10 and 15 kPa and the heat flux of 200 kW/m^2. In the following subsections the results obtained for different performance characteristics of the trapezoidal microchannel of this study are presented and discussed.

The average velocity through different microchannels

In this section, initially the effect of volume friction of nanoparticles on the average velocity of the nanofluid in different microchannels for four different types, but the same pressure drop of 15 kPa, is discussed. Then the effect of pressure drop variation is discussed, separately.

Table 4
Heat absorbed by water and the relative difference between the absorbed and applied heats for different heat sink types.

	D-type	C-type	B-type	A-type
Elements	673920	629640	633960	633960
Q_{flow} (W)	4.741	4.860	4.985	4.984
$\left\lvert\frac{Q_{\text{flow}} - q_w W_{\text{hs}} L_{\text{hs}}}{q_w W_{\text{hs}} L_{\text{hs}}}\right\rvert \times 100$	5.42	3.06	0.56	0.57

Effect of volume fraction on average velocity

In Figure 7, for all inlet/outlet arrangements, the average velocity of the nanofluid in different microchannels at pressure drop of 15 kPa for different volume fractions of nanoparticles has been shown. In all of the cases, with increasing the volume fraction, the viscosity of nanofluids increases, which in turn decreases the average velocity in all of the microchannels. As noticed from Figure 7, for every specified arrangement the average velocity in different microchannels is not the same. Also the maximum average velocity for the A-, B-, C- and D-type arrangements have occurred in the microchannels #3, #4, #5 and #1, respectively.

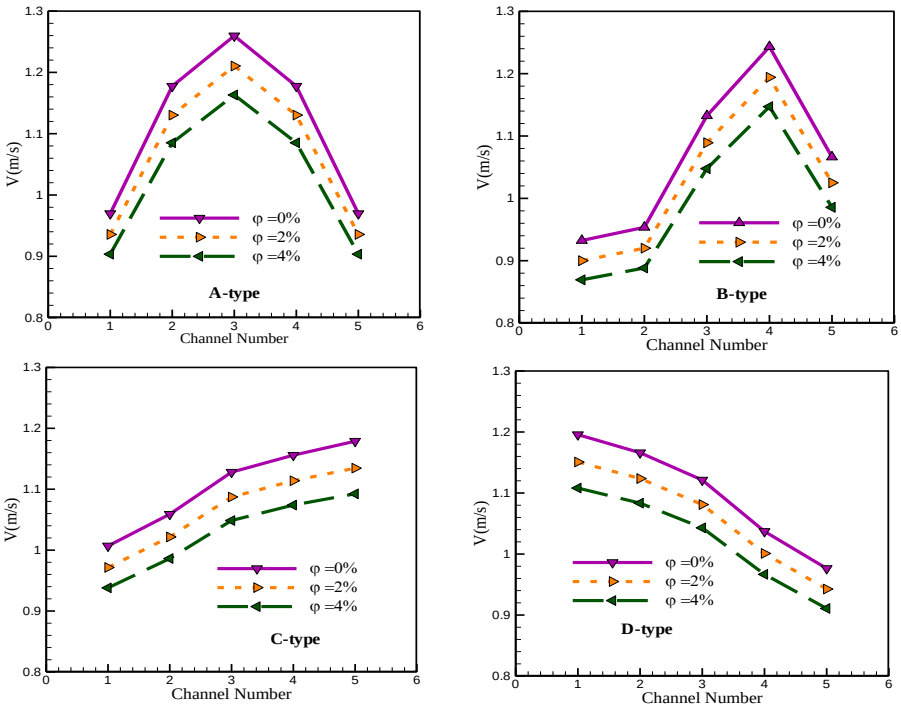


Fig. 7. Average velocity in different microchannels for ΔP=15 kPa and different volume fractions

To explain the reason for the velocity differences in different microchannels, the details of the flow in the inlet plenum for all of the arrangements, volume fractions and pressure drops have been studied. Although the flow in the inlet and outlet plenums are three dimensional, for instance the streamlines in the mid-plane of the inlet plenum at pressure drop of 15 kPa and volume fraction of zero, are shown in Figure 8 for the four selected arrangements.

As can be seen the flow pattern in the inlet plenum for every inlet arrangement is distinct and the details of the creation of recirculation zones, in terms of location and size, are also different. For the A-type arrangement, two strong recirculation zones are formed at the left and right sides of the inlet stream to the inlet plenum. These are the main cause of pressure drop as flow expands in the inlet plenum. However, for the A-type arrangement, the microchannel #3 is in the direction of the entering flow, but out of the recirculation zones at the left and right sides of the plenum. Thus, the pressure drop from the inlet to the entry to microchannel #3 is smaller, compared to that for other microchannels.

As a result, the average velocity in the microchannel #3 is more than that of other microchannels. Also for the A-type arrangement, due to symmetry of the recirculation zones formed in the inlet plenum, the average velocity of nanofluid passing through the microchannels #1 and #2 is exactly the same as those of microchannels #5 and #4, respectively.

For the B-type arrangement, for which the entrance is at the right hand side of the north wall, a strong recirculation has formed at the left side of the inlet plenum. However, the microchannel #4 is alongside the heat sink entrance and the pressure drop in the plenum from the inlet to the entrance of the microchannel #4 is the minimum; thus the maximum average velocity has occurred in microchannel #4. For the C and D-type arrangements, for which the flow enters the inlet plenum from the western and eastern walls, respectively, part of the entering flow collides with the opposite wall. Three weak recirculation zones form at the upper side of the inlet plenum; also a weak recirculation zone forms in the lower part of the plenum beneath the inlet.

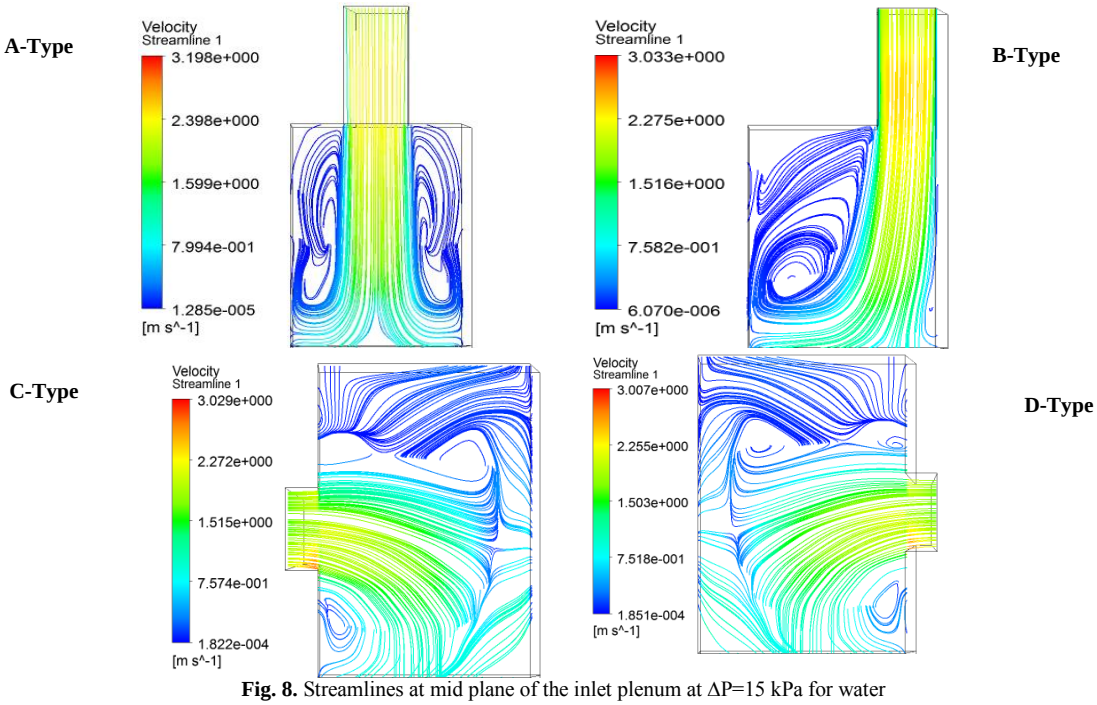


Fig. 8. Streamlines at mid plane of the inlet plenum at ΔP=15 kPa for water

Therefore, for the C and D-type inlet/outlet arrangements the pressure drop in the inlet plenum for the microchannels farther from the entrance is less; thus for them the maximum average velocity has occurred in the microchannels #5 and #1, respectively.

Effect of pressure drop on average velocity

Effect of pressure drop on the average velocity shows a similar trend, irrespective of volume fraction of nanoparticles.

As an instance, the average nanofluid velocity in different microchannels at pressure drop of 5, 10 and 15 kPa for the four studied inlet/outlet arrangements has been shown in Figure 9, for volume fraction of 4%. By reducing the pressure drop, the overall mass flow rate reduces, so the input flow rate into each microchannel decreases.

However, as the pressure drop increases, the secondary flow in the inlet and outlet plenums amplifies and as a result the difference between the maximum and minimum velocity in different microchannels enhances.

As indicated in Figure 9, the average velocity in different microchannels is in the range of 0.41-1.16 m/s, so the Reynolds number based on the microchannel hydraulic diameter is between 93 and 291. This verifies the validity of the assumption of laminar flow in the microchannels. The hydrodynamic entrance length for laminar flow is calculated using the following approximation as (46):

$$x_{fd,h} = 0.05 Re D_h \tag{32}$$

The hydrodynamic entrance length of the microchannel #3 at pressure drop of 15 kPa and volume fraction of 4% for the A, B, C and D-type inlet/outlet arrangements is 2.8, 2.5, 2.6 and 2.6 mm, respectively. It shows that the developing region is limited to less than 30% of the microchannel length; thus the flow regime along most of the microchannel length is fully developed.

The flow average temperature in different microchannels

In this section, initially the effect of volume friction of nanoparticles on average temperature of the flow in different microchannels for four different arrangements but a same pressure drop of 10 kPa is discussed. Then the effect of pressure drop on average temperature is discussed, individually.

Effect of volume fraction on nanofluid average temperature

Figure 10 shows the average flow temperature in different microchannels for pressure drop of 10 kPa but different volume fraction of nanoparticles.

The viscosity of nanofluid increases with increasing volume fraction.

So at a constant pressure drop, with increasing volume fraction the velocity decreases, thus in general the average fluid temperature increases in all of the microchannels.

Also with increasing volume fraction, due to increased conductivity of the nanofluid, heat transfer improves and leads to the average fluid temperature increase.

For the A-type heat sink, the maximum and minimum temperatures occur in microchannels #1 (and #5) and #3, in which the minimum and maximum velocities occur, respectively.

Also the maximum fluid temperature for the B, C and D-type heat sinks occur in the microchannels #1, #1 and #5, respectively. It should be noted that, due to more heat received from the side walls, the average flow temperature in the microchannels near the heat sink side walls is more than that of the adjacent one.

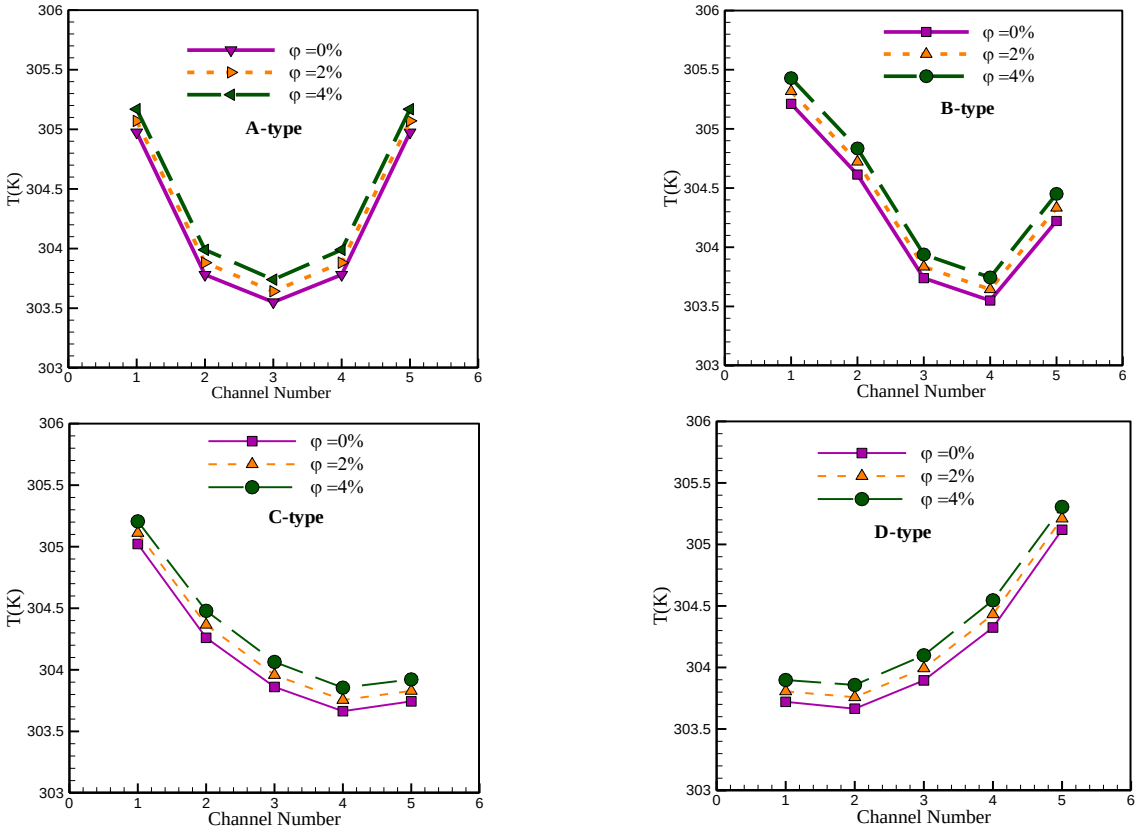


Fig. 10. Average flow temperature in different microchannels for pressure drop of 10 kPa and different inlet/outlet arrangements

Effect of pressure drop on average temperature

Effect of pressure drop on the flow average temperature in different microchannels was studied and a similar trend was observed for different volume fraction of nanoparticles. As an instance, Figure 11 shows the average flow temperature for the four selected inlet/outlet arrangements and pressure drops of 5, 10 and 15 kPa, when nanofluid with volume fraction of 4% has been utilized as the working fluid.

As shown in Figure 11, with increasing pressure drop the average temperature in all of microchannels decreases for all of the nominated arrangements. This is due to mass flow rate increase with pressure drop enhancement. It is noticed again that, for all of inlet/outlet arrangements, the average flow temperature in the microchannels near the heat sink lateral walls is more than that of the adjacent one.

Temperature distribution in solid parts

In order to quantify the performance of the heat sink in every experimental study the temperature distribution in the solid parts particularly on the surface of the base plate must be measured.

However, it is usually difficult to measure temperature distribution even on the surface of the base plate since it is bonded with the chip surface or the heat spreader.

By taking the advantage of the results of the numerical simulation, temperature distribution on the heat sink base plate surface and in the rest of solid parts for different conditions in terms of inlet/outlet arrangement, volume fractions and pressure drops wre studied.

Temperature distribution on the base plate of MCHS

As an instance, the temperature distribution on the base plate of MCHS is presented in Figure 12 for the four nominated types of inlet/outlet arrangements, volume fraction of 2% and ΔP=15 kPa. As noticed the detail of temperature distribution depends on the inlet/outlet arrangement, such that for the A and B type heat sinks, for which the entry is direct from the north wall, the region near the north wall is generally at lower temperature than

the C and D types. Moreover the base plate in the A and B-type heat sinks enjoys from a more uniform temperature distribution compared to those of the C and D types. This issue will be discussed in subsection 7.6.3 quantitatively.

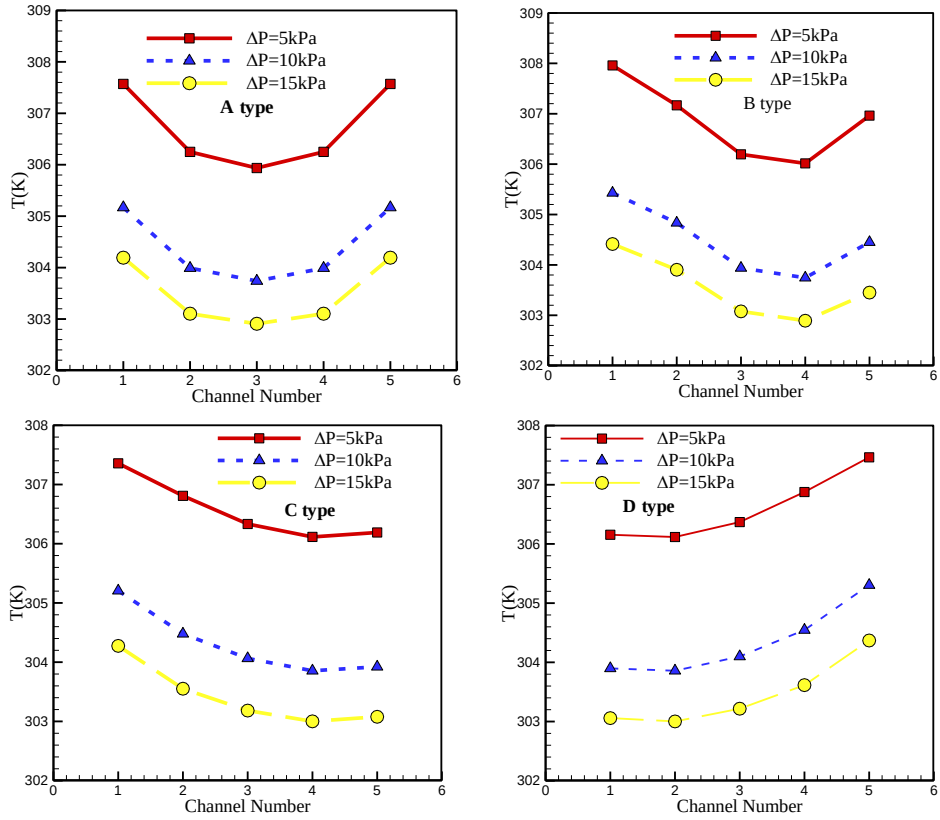


Fig. 11. The flow average temperature in different microchannels for nanofluid with volume fraction of 4%

Also for all of the inlet/outlet arrangements, the top and bottom corners of the base plate are at relatively higher temperatures, since there is no heat dissipation by fluid convection over there. Moreover, a low temperature region occurs at the entrance region to the microchannels, because the coolant temperature is lower and the heat transfer coefficient in the entrance zone of the microchannels is higher.

Temperature distribution in the solid part

The temperature distribution in the three dimensional solid parts of different heat sinks types has been studied. As an instance, in Figure 13 the temperature distribution is shown for pressure drop of 10 kPa and nanofluid with volume fraction of 4%. As seen from Figure 13, the temperature distribution in the solid part is non-uniform, but the degree of this non-uniformity depends on the type of inlet/outlet arrangement.

The highest difference between the maximum and minimum temperatures of the solid part has occurred for the D-type heat sink and the lowest for the A-type, indicating that the A-type heat sink is better than the D-type as well as the other two types. It is observed that, due to the absence of the heat removing microchannels at the head or end of MCHS, hot regions occur at the end corners of the heat sink.

However, for the A and B-type heat sinks, for which the flow enters from the north wall and exits from the south wall, the head region of the solid part is generally at lower temperature compared with its end. Whereas, for the C and D types, for which the flow enters from one of the lateral walls, the solid head and end parts both are at higher temperatures compared with the rest. Also, for all of the inlet/outlet arrangements, the low-temperature region has occurred at the beginning of the microchannels, where the fluid is at its lowest temperature and the heat transfer coefficient is greater.

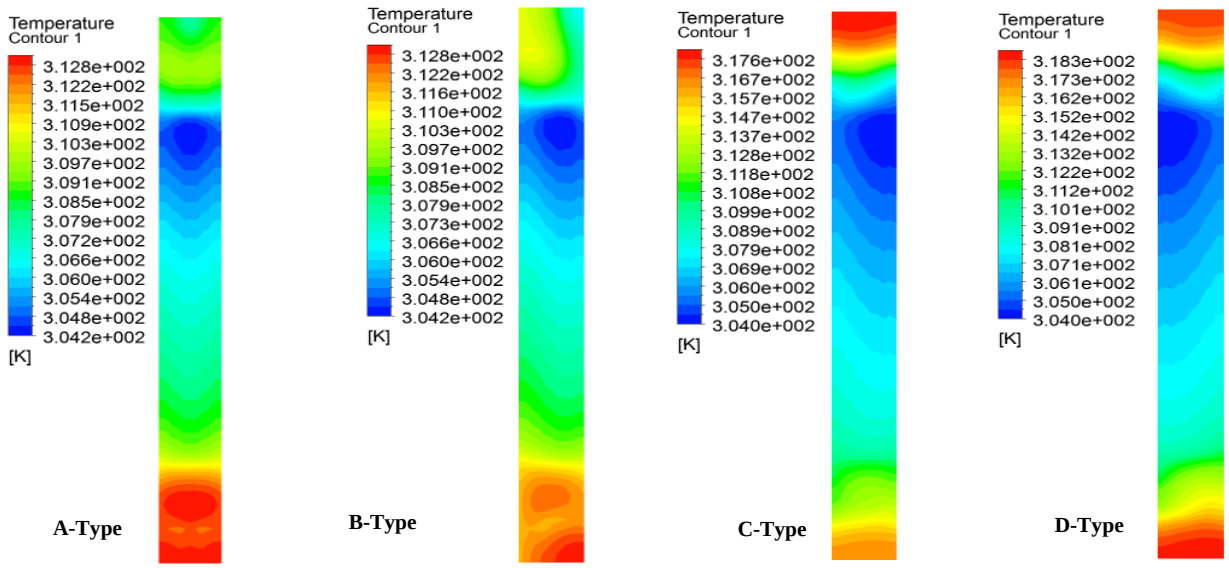


Fig. 12. Temperature distribution on the base plate surface of MCHS for nanofluid with volume fraction of 2% and ΔP=15 kPa

Effect of the Brownian motion on MCHS performance evaluation indexes

Brownian motion of nanoparticles is a key mechanism in thermal conductivity enhancement. Many researchers have reported an apparent increase in heat transfer performance due to Brownian motion of nanoparticles(20, 52). In order to study the effect of Brownian motion on heat transfer, thermal resistance and non-uniformity of the base plate temperature (θ) solutions were obtained for the cases for which the dynamic parts in equations 13 and 18 were not considered. Also to compare the results, the following three parameters were defined as:

$$\eta_1 = \frac{Nu_{av,Brownian} - Nu_{av,non\text{-}Brownian}}{Nu_{av,non\text{-}Brownian}} \times 100 \quad (33)$$

$$\eta_2 = \frac{R_{th,non\text{-}Brownian} - R_{th,Brownian}}{R_{th,non\text{-}Brownian}} \times 100 \quad (34)$$

$$\eta_3 = \frac{\theta_{non\text{-}Brownian} - \theta_{Brownian}}{\theta_{non\text{-}Brownian}} \times 100 \quad (35)$$

In Tables 5, 6 and 7 the values of η_1, η_2 and η_3 have been presented for the four nominated inlet/outlet arrangements, respectively, but only for pressure drop of 15 kPa and volume fraction of 4%.

As seen from Table 5, the Brownian motion of nanoparticles increases the heat transfer rate. The Brownian motion increases the effective conductivity of the nanofluid and, as Seyf and Nikaaein (52) showed, improves the heat transfer rate. Also Tables 6 and 7 show that Brownian motion has a desirable result on two other heat sink indexes, such that it decreases the thermal resistance as well as θ.

To sum up, for volume fraction of 4% considering Brownian motion compared to ignoring it has increased the heat transfer between 0.66% and 0.89%, has decreased the thermal resistance between 0.26% and 0.78% and has decreased θ between 0.22% and 0.44%.

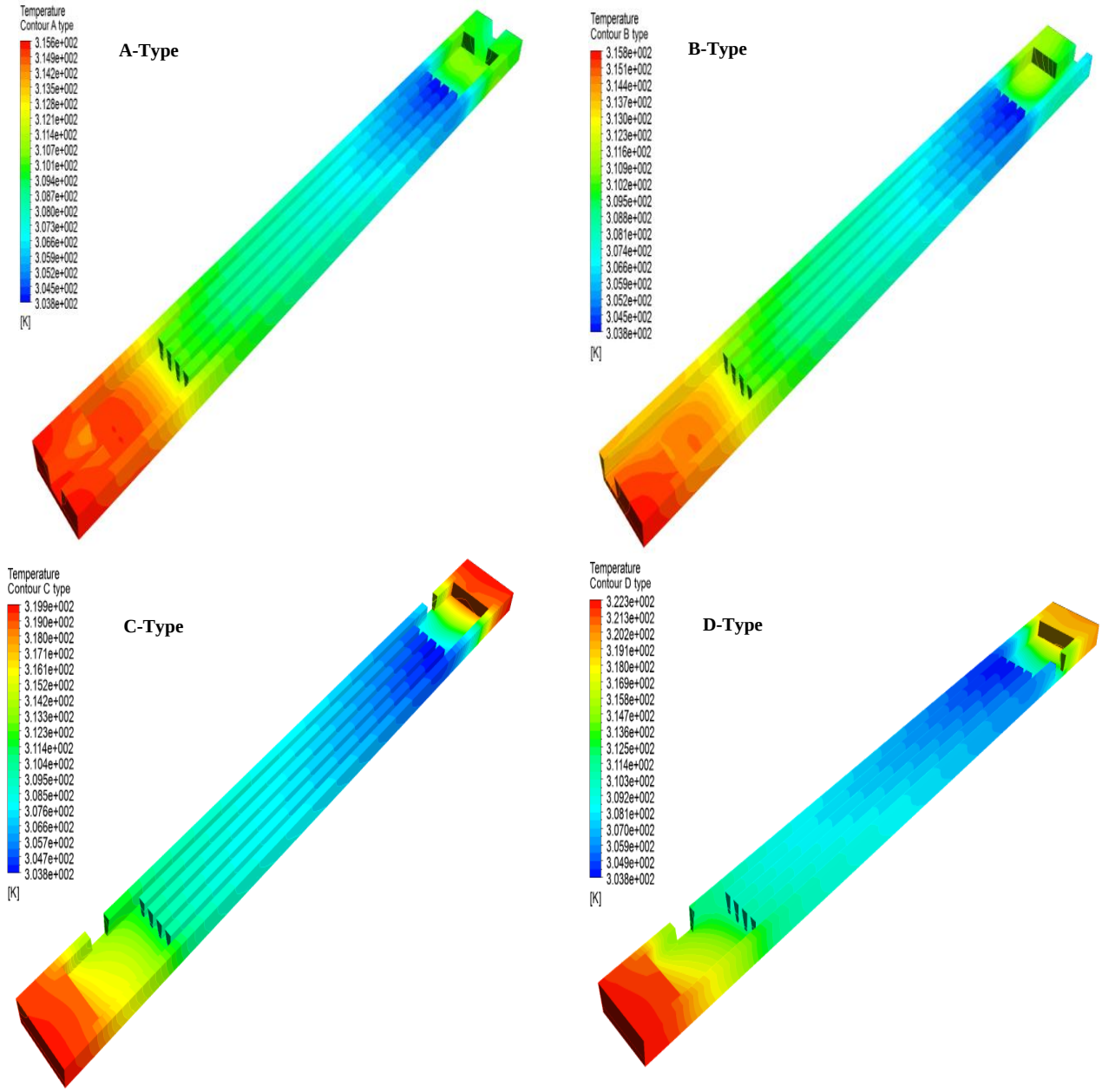


Fig. 13. Temperature distribution in the solid parts of MCHS for nanofluid with volume fraction of 4% and ΔP=10 kPa.

In Tables 5, 6 and 7 the values of η_1, η_2 and η_3 have been presented for the four nominated inlet/outlet arrangements, respectively, but only for pressure drop of 15 kPa and volume fraction of 4%. As seen from Table 5, the Brownian motion of nanoparticles increases the heat transfer rate. The Brownian motion increases the effective conductivity of the nanofluid and, as Seyf and Nikaaein (52) showed, improves the heat transfer rate. Also Tables 6 and 7 show that Brownian motion has a desirable result on two other heat sink indexes, such that it decreases the thermal resistance as well as θ. To sum up, for volume fraction of 4% considering Brownian motion compared to ignoring it has increased the heat transfer between 0.66% and 0.89%, has decreased the thermal resistance between 0.26% and 0.78% and has decreased θ between 0.22% and 0.44%.

Effect of temperature-dependent properties on performance evaluation indexes of MCHS

To study the effects of variation of properties on overall thermal performance of the MCHS solutions were obtained for all of the nominated cases, for which both temperature-dependent properties as well as temperature-independent properties at 300 K were utilized. In Tables 8, 9 and 10 the values of average Nusselt number, thermal resistance and non-uniformity of the base plate temperature have been presented for the four selected arrangements, but only for pressure drop of 15 kPa and volume fraction of 4%.

Table 5
Nusselt number for the cases with and without considering Brownian motion for ΔP=15 kPa and φ=4%.

Average Nusselt number	A-type	B-type	C-type	D-type
With Brownian motion	15.87	15.81	10.64	10.38
Without Brownian motion	15.73	15.68	10.57	10.31
η_1 (%)	0.89	0.83	0.66	0.68

Table 6
Thermal resistance for the cases with and without considering Brownian motion for ΔP=15 kPa and φ=4%.

Thermal resistance	A-type	B-type	C-type	D-type
With Brownian motion	2.56	2.58	3.60	3.77
Without Brownian motion	2.58	2.59	3.61	3.78
η_2 (%)	0.78	0.39	0.28	0.26

Table 7
Theta for the cases with and without considering Brownian motion for ΔP=15 kPa and φ=4%.

Theta	A-type	B-type	C-type	D-type
With Brownian motio	4.48e-5	4.52e-5	7.04e-5	7.44e-5
Without Brownian motion	4.50e-5	4.53e-5	7.06e-5	7.46e-5
η_3 (%)	0.44	0.22	0.28	0.27

Table 8
Average Nusselt number for temperature-dependent and independent properties for ΔP=15 kPa and $\varphi = 4\%$.

Average Nusselt number	A-type	B-type	C-type	D-type
With temperature-dependent properties	15.87	15.81	10.64	10.38
With temperature-independent properties	15.41	15.36	10.36	10.04
Relative difference (%)	2.99	2.93	2.70	3.39

Table 9
Thermal resistance for temperature-dependent and independent properties for ΔP=15 kPa and $\varphi = 4\%$.

Thermal resistance	A-type	B-type	C-type	D-type
With temperature-dependent properties	2.56	2.68	3.60	3.76
With temperature-independent properties	2.72	2.86	3.73	4.00
Relative difference (%)	5.88	6.29	3.49	6.00

The results show that using the temperature-dependent properties instead of temperature-independent properties has desirable effect on thermal performance of the heat sink. The use of temperature-dependent properties for volume fraction of 4% has increased the heat transfer between 2.7% and 3.39%, has decreased the thermal resistance between 3.49% and 6.29 % and has decreased θ between 3.3% and 7.19%.

Table 10
Theta for temperature-dependent and independent properties for ΔP=15 kPa and $\varphi = 4\%$.

Theta	A-type	B-type	C-type	D-type
With temperature-dependent properties	4.48e-5	4.52e-5	7.04e-5	7.44e-5
With temperature-independent properties	4.80e-5	4.87e-5	7.28e-5	7.96e-5
Relative difference (%)	6.67	7.19	3.30	6.53

Effect of inlet/outlet arrangement on overall thermal performance of MCHS

To evaluate the overall performance of the heat sinks with different inlet/outlet arrangements the results obtained for average Nusselt number, thermal resistance and the ratio of difference between the maximum and minimum base plate temperatures to the heat flux (θ) are discussed in the following sub-sections.

Average Nusselt number

Figure 13 shows the average Nusselt number in terms of pressure drop for various types of heat sinks. As indicated in Figure 14 for a constant pressure drop, the average Nusselt number increases with increasing volume fraction for all of the heat sink types. Although the mass flow rate decreases with volume fraction improvement, due to conductivity increase the Nusselt number enhances. For a constant volume fraction, with enhancement of the pressure drop the mass flow rate of the nanofluid increases and the average fluid temperature decreases. As a result the average Nusselt number increases. Yue et al. (16) used KKL Brownian motion model for Al_2O_3-water nanofluid in a manifold microchannel heat sink and showed the average Nusselt number and pumping power ($\dot{V}\Delta P$) increase with increasing volume fraction. As seen from Figure 14, in terms of the average Nusselt number the A-type heat sink is the best among the nominated types.

Thermal resistance

As seen from Figure 15, which shows the change of thermal resistance with pressure drop, for a constant volume fraction with increasing pressure drop the thermal resistance decreases for all of the heat sink types. With increasing pressure drop, the average velocity of the nanofluid rises and, as seen in Figure 14, the heat transfer coefficient as well as the average Nusselt number enhance; thus both of the average fluid temperature and the average solid temperature decrease and according to Eq. (29), the thermal resistance decreases either. Seyf and Nikaaein (52)

also showed that the variation of thermal resistance is dependent on the operational conditions of the heat sink. As Figure 15 shows, for a similar operating condition the thermal resistance of the A-type heat sink is less than those of the B-, C-, and D-types.

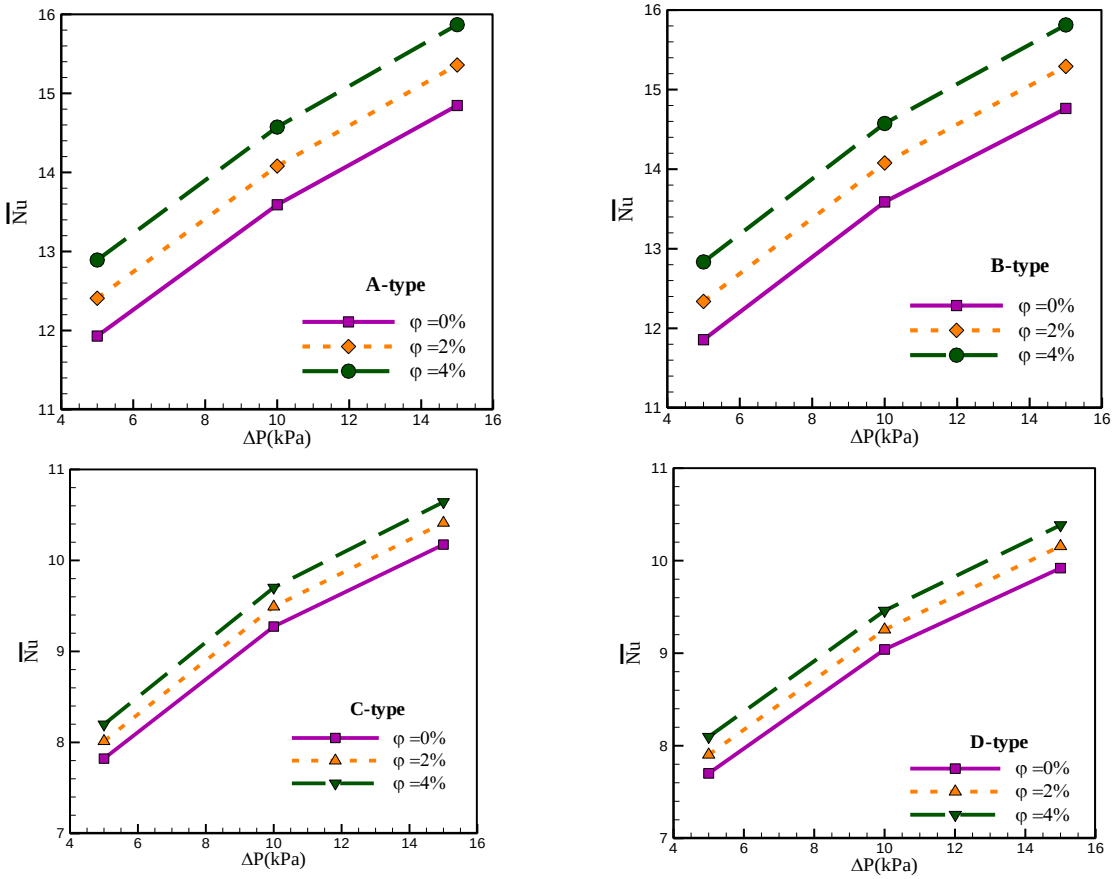


Fig. 14. Variation of average Nusselt number with pressure drop for various inlet/outlet arrangements and different volume fractions.

Theta

The temperature distribution on the base plate of the selected MCHS has been studied for all of the conditions presumed. As an instance, θ has been shown in Table 11 for different inlet/outlet arrangements and pressure drops, but for volume fraction of 4%. As pressure drop increases, the mas flow rate enhances and the coolant velocity increases, which in turn increases the heat transfer rate. As a result in overall the base plat temperature drops and its distribution becomes more uniform and, as seen from Table 11, θ decrease. Also it is seen from Table 11 that the A-type heat sink has a smaller θ; which indicates its better uniformity of base plate temperature.

Table 11
Variation of theta with pressure drop for $\varphi = 4\%$.

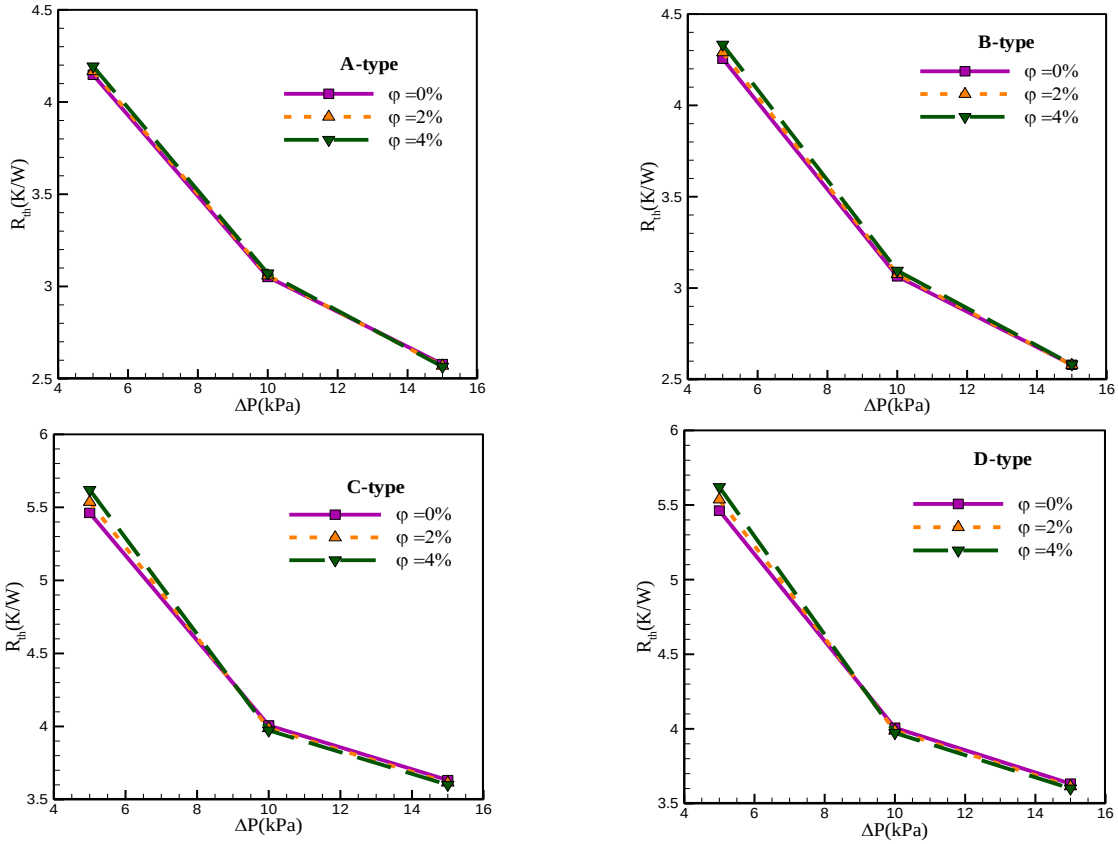
ΔP(Kpa)	A-type	B-type	C-type	D-type
5	4.48e-5	4.52e-5	7.04e-5	7.44e-5
10	4.80e-5	4.87e-5	7.28e-5	7.96e-5
15	6.67	7.19	3.30	6.53

CONCLUSION

Fluid flow and heat transfer in a trapezoidal microchannel heat sink consisting of five trapezoidal microchannels using Al_2O_3-water nanofluid have been simulated. Effect of inlet/outlet arrangements, volume fraction, pressure drop, temperature-dependent properties and Brownian motion on the average Nusselt number, thermal resistance and temperature distribution in the microchannels as well in the solid part of MCHS have been studied.

The following conclusions can be made based on the numerical results:

1. Maximum average Nusselt number, minimum thermal resistance and better uniformity of base plate temperature occur for the A-type heat sink.



2. The base plate temperature for the A- and B-type heat sinks is lower than those of the C- and D-type heat sinks.
3. The use of the nanofluid increases the average Nusselt number in overall, whereas it does not have a significant effect on the thermal resistance.
4. Considering the Brownian motion of nanoparticles, which is a key mechanism in thermal conductivity enhancement of nanofluid, has positive effect on cooling performance of the heat sink.
5. Considering temperature-dependent properties improves the heat transfer performance, such that for the cases studied the heat transfer increases between 2.7% and 3.39%, the thermal resistance decreases between 3.49% and 6.29 % and the ratio of difference between the maximum and minimum substrate temperatures to the heat flux decreases between 3.3% and 7.19%.

ACKNOWLEDGEMENTS

The authors would like to thank the energy research institute of the University of Kashan for supporting this research (Grant No. 1395/574607/2).

REFERENCES

[1] Tuckerman DB, Pease R. High-performance heat sinking for VLSI. Electron Device Letters, IEEE. 1981;2(5):126-9.

[2] Wu H, Cheng P. Friction factors in smooth trapezoidal silicon microchannels with different aspect ratios. International Journal of Heat and Mass Transfer. 2003;46(14):2519-25.

[3] Chein R, Huang G. Analysis of microchannel heat sink performance using nanofluids. Applied Thermal Engineering. 2005;25(17):3104-14.

[4] Abbassi H. Entropy generation analysis in a uniformly heated microchannel heat sink. Energy. 2007;32(10):1932-47.

[5] Niazmand H, Renksizbulut M, Saeedi E. Developing slip-flow and heat transfer in trapezoidal microchannels. International Journal of Heat and Mass Transfer. 2008;51(25):6126-35.

[6] Shams M, Shojaeian M, Aghanajafi C, Dibaji S. Numerical simulation of slip flow through rhombus microchannels. International Communications in Heat and Mass Transfer. 2009;36(10):1075-81.

[7] Chein R, Chen J. Numerical study of the inlet/outlet arrangement effect on microchannel heat sink performance. International Journal of Thermal Sciences. 2009;48(8):1627-38.

[8] Hung T-C, Yan W-M. Effects of tapered-channel design on thermal performance of microchannel heat sink. International Communications in Heat and Mass Transfer. 2012;39(9):1342-7.

[9] Izadi M, Shahmardan M, Rashidi A. Study on Thermal and Hydrodynamic Indexes of a Nanofluid Flow in a Micro Heat Sink. Transport Phenomena in Nano and Micro Scales. 2013;1(1):53-63.

[10] Rahim Mashaei P, Hosseinalipour S, El Jawad Muslmani M. The Impact of Nanoparticles on Forced Convection in a Serpentine Microchannel. Transport Phenomena in Nano and Micro Scales. 2014;2(2):86-99.

[11] Ting TW, Hung YM, Guo N. Entropy generation of nanofluid flow with streamwise conduction in microchannels. Energy. 2014;64:979-90.

[12] Vinodhan VL, Rajan K. Computational analysis of new microchannel heat sink configurations. Energy Conversion and Management. 2014;86:595-604.

[13] Fani B, Kalteh M, Abbassi A. Investigating the effect of Brownian motion and viscous dissipation on the nanofluid heat transfer in a trapezoidal microchannel heat sink. Advanced Powder Technology. 2015;26(1):83-90.

[14] Duryodhan V, Singh A, Singh S, Agrawal A. Convective heat transfer in diverging and converging microchannels. International Journal of Heat and Mass Transfer. 2015;80:424-38.

[15] Dehghan M, Daneshipour M, Valipour MS, Rafee R, Saedodin S. Enhancing heat transfer in microchannel heat sinks using converging flow passages. Energy Conversion and Management. 2015;92:244-50.

[16] Yue Y, Mohammadian SK, Zhang Y. Analysis of performances of a manifold microchannel heat sink with nanofluids. International Journal of Thermal Sciences. 2015;89:305-13.

[17] Vanapalli S, Ter Brake H, Jansen H, Burger J, Holland H, Veenstra T, et al. Pressure drop of laminar gas flows in a microchannel containing various pillar matrices. Journal of Micromechanics and Microengineering. 2007;17(7):1381.

[18] Buonomo B, Manca O, Lauriat G. Forced convection in micro-channels filled with porous media in local thermal non-equilibrium conditions. International Journal of Thermal Sciences. 2014;77:206-22.

[19] Aghaei A, Sheikhzadeh GA, Dastmalchi M, Forozande H. Numerical investigation of turbulent forced-convective heat transfer of Al 2 O 3–water nanofluid with variable properties in tube. Ain Shams Engineering Journal. 2015;6(2):577-85.

[20] Li J, Peterson G. Geometric optimization of a micro heat sink with liquid flow. Components and Packaging Technologies, IEEE Transactions on. 2006;29(1):145-54.

[21] Lin L, Chen Y-Y, Zhang X-X, Wang X-D. Optimization of geometry and flow rate distribution for double-layer microchannel heat sink. International Journal of Thermal Sciences. 2014;78:158-68.

[22] Türkakar G, Okutucu-Özyurt T. Dimensional optimization of microchannel heat sinks with multiple heat sources. International Journal of Thermal Sciences. 2012;62:85-92.

[23] Nonino C, Del Giudice S, Savino S. Temperature-dependent viscosity and viscous dissipation effects in microchannel flows with uniform wall heat flux. Heat Transfer Engineering. 2010;31(8):682-91.

[24] Mital M. Semi-analytical investigation of electronics cooling using developing nanofluid flow in rectangular microchannels. Applied Thermal Engineering. 2013;52(2):321-7.

[25] Prasher R, Song D, Wang J, Phelan P. Measurements of nanofluid viscosity and its implications for thermal applications. Applied Physics Letters. 2006;89(13):133108.

[26] Kadam ST, Kumar R. Twenty first century cooling solution: Microchannel heat sinks.

International Journal of Thermal Sciences. 2014;85:73-92.

[27] Schroeder SP, Morris GK, editors. Nanofluids in a forced-convection liquid cooling system-benefits and design challenges. Thermal and Thermomechanical Phenomena in Electronic Systems (ITherm), 2010 12th IEEE Intersociety Conference on; 2010: IEEE.

[28] Kazemi-Beydokhti A, Heris SZ. Thermal optimization of combined heat and power (CHP) systems using nanofluids. Energy. 2012;44(1):241-7.

[29] Ali HM, Ali H, Liaquat H, Maqsood HTB, Nadir MA. Experimental investigation of convective heat transfer augmentation for car radiator using ZnO–water nanofluids. Energy. 2015;84:317-24.

[30] Zadeh PM, Sokhansefat T, Kasaeian A, Kowsary F, Akbarzadeh A. Hybrid optimization algorithm for thermal analysis in a solar parabolic trough collector based on nanofluid. Energy. 2015;82:857-64.

[31] Boyaghchi FA, Chavoshi M, Sabeti V. Optimization of a novel combined cooling, heating and power cycle driven by geothermal and solar energies using the water/CuO (copper oxide) nanofluid. Energy. 2015;91:685-99.

[32] He Q, Wang S, Zeng S, Zheng Z. Experimental investigation on photothermal properties of nanofluids for direct absorption solar thermal energy systems. Energy Conversion and Management. 2013;73:150-7.

[33] Schuller M, Shao Q, Lalk T. Experimental investigation of the specific heat of a nitrate–alumina nanofluid for solar thermal energy storage systems. International Journal of Thermal Sciences. 2015;91:142-5.

[34] Kandlikar S, Garimella S, Li D, Colin S, King MR. Heat transfer and fluid flow in minichannels and microchannels: elsevier; 2005.

[35] Li J, Peterson G, Cheng P. Three-dimensional analysis of heat transfer in a micro-heat sink with single phase flow. International Journal of Heat and Mass Transfer. 2004;47(19):4215-31.

[36] Xuan Y, Roetzel W. Conceptions for heat transfer correlation of nanofluids. International Journal of heat and Mass transfer. 2000;43(19):3701-7.

[37] Khanafer K, Vafai K. A critical synthesis of thermophysical characteristics of nanofluids. International Journal of Heat and Mass Transfer. 2011;54(19):4410-28.

[38] Koo J, Kleinstreuer C. A new thermal conductivity model for nanofluids. Journal of Nanoparticle Research. 2004;6(6):577-88.

[39] Li J, Kleinstreuer C. Thermal performance of nanofluid flow in microchannels. International Journal of Heat and Fluid Flow. 2008;29(4):1221-32.

[40] Hamilton R, Crosser O. Thermal conductivity of heterogeneous two-component systems. Industrial & Engineering chemistry fundamentals. 1962;1(3):187-91.

[41] Li J. Computational Analysis of Nanofluid Flow in Microchannels with Applications to Micro-heat Sinks and Bio-MEMS: ProQuest; 2008.

[42] Prasher R, Bhattacharya P, Phelan PE. Brownian-motion-based convective-conductive model for the effective thermal conductivity of nanofluids. Journal of heat transfer. 2006;128(6):588-95.

[43] Jang SP, Choi SU. Effects of various parameters on nanofluid thermal conductivity. Journal of heat transfer. 2007;129(5):617-23.

[44] Yang Y, Zhang ZG, Grulke EA, Anderson WB, Wu G. Heat transfer properties of nanoparticle-in-fluid dispersions (nanofluids) in laminar flow. International Journal of Heat and Mass Transfer. 2005;48(6):1107-16.

[45] Brinkman H. The viscosity of concentrated suspensions and solutions. The Journal of Chemical Physics. 1952;20(4):571.

[46] Bergman TL, Incropera FP, Lavine AS. Fundamentals of heat and mass transfer: John Wiley & Sons; 2011.

[47] Glassbrenner C, Slack GA. Thermal conductivity of silicon and germanium from 3 K to the melting point. Physical Review. 1964;134(4A):A1058.

[48] Alloui Z, Vasseur P, Reggio M. Natural convection of nanofluids in a shallow cavity heated from below. International journal of Thermal sciences. 2011;50(3):385-93.

[49] Chai L, Xia G, Zhou M, Li J, Qi J. Optimum thermal design of interrupted microchannel heat sink with rectangular ribs in the transverse microchambers. Applied Thermal Engineering. 2013;51(1):880-9.

[50] Phillips RJ. Microchannel Heat Sinks. Lincoln Laboratory Journal. 1988;1(1).

[51] Chein R, Chuang J. Experimental microchannel heat sink performance studies using nanofluids. International Journal of Thermal Sciences. 2007;46(1):57-66.

[52] Seyf HR, Nikaaein B. Analysis of Brownian motion and particle size effects on the thermal behavior and cooling performance of microchannel heat sinks. International Journal of Thermal Sciences. 2012;58:36-44.